

## Chapter 5

### The thermal conductivity of strained graphene

Several aspects of the atypical thermal conductivity of graphene have been attributed to the out of plane acoustic (ZA) phonons. These aspects conflict to the point that if the ZA phonons were a person, they might be characterized as productive egomaniacs. On one hand, they are believed to enable graphene's very high thermal conductivity by contributing more than 70% of the thermal conductivity of suspended graphene (Lindsay et al., 2010). On the other hand, they are thought to suppress the potentially divergent thermal conductivity contributions from the in plane acoustic phonons (Pereira and Donadio, 2013; Bonini et al., 2012). Both of these opposing contributions are linked to the abnormal quadratic dispersion of the ZA phonons, and are experimentally based solely on the measured decreased thermal conductivity of supported graphene. Here we further test these predictions using strain and pressure to modify the ZA phonons while measuring the thermal conductivity. We observe no absolute indications that either strain or pressure affect the thermal transport in the atypical ways which might be expected for ZA phonon dominated transport. This information should help us understand the importance of the ZA phonons and further test our understanding of graphene's high thermal conductivity.

We begin by describing past experimental measurements of graphene's thermal conductivity with emphasis on the diminished thermal conductivity of supported graph-

ene. Next, we review the theoretical explanation of this observation and summarize the predicted effect of strain. Finally, we discuss our experimental measurements starting with a description of the measurement, followed by an explanation of the data analysis, and finishing with a discussion of our results.

### 5.1 Experimental background

In the first measurements of graphene's thermal conductivity, Balandin and coworkers reported a record high thermal conductivity of roughly 5000 W/m-K (Balandin et al., 2008) in suspended graphene. Shortly thereafter measurements of supported graphene showed a more modest thermal conductivity of roughly one six of the original value (Seol et al., 2010). This discrepancy has been the source of ~~heavy study~~<sup>in</sup> ~~several studies~~ since. [refs?]

The original measurements were performed on suspended graphene samples using an optical technique. This creative technique uses a laser excitation to heat the sample and the temperature induced energy shift of the Raman scattered light to measure temperature. The laser excitation provides both a heat source and a thermometer. When used in conjunction with a heat transfer model, this is enough to determine the thermal conductivity. This technique has advantages and disadvantages. The required samples are very simple to fabricate and the measurement is fairly standard. However, the measured thermal conductivity depends on a variety of hard to measure parameters including the optical absorption of the graphene, the laser spot size, and the temperature dependence of the phonon modes. What's more, the results depend on the accuracy of diffusive thermal transport models which cannot account for ballistic transport phenomena. Nonetheless, the simplicity of this technique has motivated its use in studying aspects of thermal transport in suspended FLG (Balandin et al.,

2008; Faugeras et al., 2010; Cai et al., 2010; Ghosh et al., 2010; Lee et al., 2011; Chen et al., 2011; Chen et al., 2012) including this work.

*and* The Raman measurement technique has ~~since~~ been advanced in a series of publications. Faugeras *et al.* showed that the symmetry of graphene over a circular microchamber simplifies the heat transfer model. Additionally, they validated the use of phonon energy shifts as a temperature measurement by using the Raman Stokes to anti-Stokes ratio as an independent measurement (Faugeras et al., 2010). Cai *et al.* advanced the thermal transport model by including the heat transfer to the substrate instead of treating the edge of the microchamber as a heat sync. Chen *et al.* included thermal conductivity to the surrounding gas but not the substrate (Chen et al., 2011). As described in Appendix D, the thermal model used to interpret our results combines the models in these works.

The more modest value for the thermal conductivity of supported graphene was measured with a different technique (Seol et al., 2010). The measurement was direct; it used resistive heaters to create temperature gradients and solid state thermometers to measure the temperature. The thermal conductivity was then determined directly from the thermal resistance of the graphene. Although this technique has less error sources, the measurements and sample fabrication are much more difficult. As a result, there has been only one other measurement of the thermal conductivity of graphene using this technique (Jang et al., 2010).

Figure 5.1 summarizes all of the reported room temperature thermal conductivity measurements of single layer graphene. It is clear that graphene's thermal conductivity is negatively effected by the presence of a supporting or encasing bulk material. The thermal conductivity decrease from a value of roughly 2000 W/m-K for suspended graphene, to a value close to 500 W/m-K for graphene supported on one side, to a value of less than 160 W/m-K for graphene encased in SiO<sub>2</sub> (Jang et al., 2010). The

This section  
seen to come  
too late

different thermal conductivities cannot be attributed to the different measurement techniques. A nanoscale thermal conductivity measurement also observed suppressed thermal conductivity in supported FLG (Pumarol et al., 2012). The observation of suppressed conductivity has driven the theoretical work described in the next section.

### 5.1.1 Theoretical background

Lindsay and coworkers argue that ZA phonon dominated thermal conductivity in suspended graphene explains the observed environmental dependence of the thermal conductivity. They argue that the large, 70 %, contribution of the ZA phonons comes about for two reasons. First, the quadratic dispersion of the ZA phonons gives them a higher density of states throughout the BZ than linearly dispersed in plane phonons. Second, the in plane reflection symmetry provides a selection rule that limits the scattering phase space (Lindsay et al., 2010). ZA phonon dominated thermal transport is consistent with the observed suppression of the thermal conductivity in supported graphene. When the graphene is in contact with bulk materials the ZA phonons either leak into the surrounding media, are scattered by it, or are damped by it thereby lowering the thermal conductivity.

The ZA phonons are also believed to limit the potentially divergent thermal conductivity contribution of the in plane phonons. Klemens showed that the linear in plane acoustic phonons should contribute a logarithmically divergent thermal conductivity in graphene (Klemens, 2001). This divergence follows from the frequency dependence of the terms which make up the thermal conductivity,  $\kappa = \frac{1}{3} \int C v_G l(\omega) \rho(\omega) d\omega$ , where  $\kappa$  is the thermal conductivity,  $C$  is the specific heat,  $v_G$  is the group velocity of the acoustic phonons,  $l(\omega)$  is the scattering length, and  $\rho(\omega)$  is the density of states. For a two dimensional phonon gas with linear dispersion,  $\rho(\omega) \propto \omega$ ; while for anharmonic scattering between linear acoustic phonons,  $l(\omega) \propto 1/\omega^2$ . Hence, in the absence

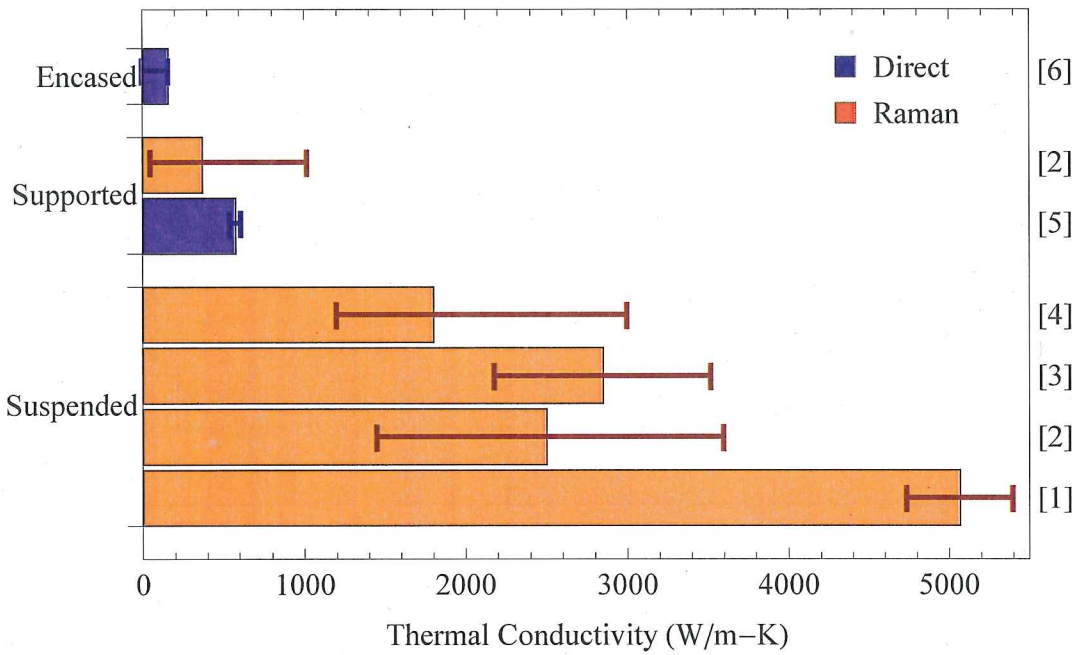


Figure 5.1: Summary of the reported values of the room temperature thermal conductivity of monolayer graphene grouped by the environment of the graphene: Suspended, supported on a bulk substrate, and encased in amorphous SiO<sub>2</sub>. The color code indicates whether the measurements were performed using the Raman technique or a direct technique. The numbers on the right indicate the source: [1] is (Balandin et al., 2008), [2] is (Cai et al., 2010), [3] is (Chen et al., 2011), [4] is (Lee et al., 2011), [5] is (Seol et al., 2010), [6] is (Jang et al., 2010). Error bars are taken from the literature.

of extrinsic scatterers the integrand scales as  $1/\omega$  and  $\kappa$  diverges logarithmically. The logarithmic divergence in  $\omega$  should translate to a logarithmic divergence in device size (Klemens, 2001). Larger devices should exhibit larger thermal conductivities because they support more of the long wavelength phonons that contribute strongly to the thermal conductivity. To date this logarithmic divergence has not been observed (Chen et al., 2011).

Pereira and coworkers believe that the ZA phonons suppress this divergence. When these ZA phonons are neglected in equilibrium molecular dynamics simulations, the thermal conductivity diverges in agreement with Klemens; when they are included, the thermal conductivity converges to a large, but finite value (Pereira and Donadio, 2013). It is believed that this is due to the ZA phonons near the center of the BZ. With near zero group velocity these phonons cannot enhance thermal conductivity, but, with a large population they can effectively scatter the in-plane phonons and eliminate the divergence. Thus, the ZA phonons are the main contributor to graphene's thermal conductivity only because the low energy ZA phonons suppress the divergent thermal conductivity of the in plane phonons.

Simulations by both Pereira (Pereira and Donadio, 2013) and coworkers and Bonini and coworkers (Bonini et al., 2012) show that strain could act to liberate the divergent thermal conductivity contribution of the in plane phonons. By linearizing the ZA phonon modes near the  $\Gamma$  point, strain decreases the density of states of the zero group velocity ZA phonons and limits the scattering of the in plane phonons. Uniaxial strain of 2 % should reduce this scattering enough to realize the divergent thermal conductivity of the in plane phonons (Pereira and Donadio, 2013) while for biaxial strain any amount of strain should be enough (Bonini et al., 2012).

## 5.2 Tuning the ZA phonon

Although the theory discussed to this point is convincing, it deserves further testing. It was built around only two data points: The high thermal conductivity of suspended graphene and the lower thermal conductivity of supported graphene. Further, the resulting theory relies on the exotic, quadratically dispersed, ZA phonons which have only been measured directly in graphene mechanical resonators. Here we take advantage of the two dimensional nature of graphene which enables additional ways to study the thermal transport.

The ZA phonons can be continuously tuned while the thermal conductivity is measured *in situ* using the device geometry from Chapter 4. The phonons are altered in two ways. First, the strain induced in pressurized graphene sealed microchambers linearizes the ZA phonon dispersion. As discussed in the previous section, this might increase the thermal conductivity by liberating the divergent thermal conductivity of the in plane phonons (Pereira and Donadio, 2013; Bonini et al., 2012). Second, the gas surrounding the suspended graphene should lower the lifetime of the ZA phonons. This has been observed in graphene mechanical resonators which exhibit decreased quality factors in ambient pressure compared to vacuum (Bunch et al., 2007). Lowering the phonon lifetime should lower their contribution to the thermal conductivity. In this section we describe our efforts to provide deeper insight into the mechanism behind the high thermal conductivity of suspended graphene by measuring the effect of strain and pressure on thermal conductivity.

### 5.2.1 Thermal measurements

The experimental geometry described in Section 4.2 not only enables the ZA phonons to be tuned, it allows allows the effects of strain and pressure to be decoupled. The

phonons are tuned by setting the external pressure,  $P$ , to gauge pressures which range from -0.1 MPa of vacuum to 0.69 MPa of overpressure using argon as a pressure transfer medium. Measuring with the external pressure both greater than and less than the pressure inside the microchamber,  $P_0$ , isolates strain and pressure effects. Pressure effects should increase monotonically with pressure while strain effects should come to a minimum when  $P = P_0$  and the graphene is flattened out. Thus, the symmetry of the observed trends about  $P_0$  allows pressure and strain effects to be decoupled.

The Raman technique described in Section 5.1 is used to measure the thermal conductivity. Linearly polarized, 514.5 nm laser light from an argon ion laser is focused on the center of the microchamber. The focused beam waist, measured the same way as was done in Section 4.1, is  $0.66 \pm 0.04$  nm. The power which reaches the sample is tuned by changing the laser power, not by changing ND filters. This ensures that the centering of the beam is not power dependent. The power which reaches the sample is calculated from the power measured at the exit port of the Renishaw by using the system throughput of  $0.67 \pm 0.01$ . The laser stability over the measurement period is 2 %. Raman spectra measured at several incident powers can be used to measure the temperature. ( via shift or Stokes/AS ? )

The temperature is measured using the heating induced shifts of the G and 2D energies:  $\Delta\omega = \chi\Delta T$ , where  $\Delta T$  is the change in temperature and  $\chi$  represents the temperature dependence arising due to anharmonicities (Bonini et al., 2007). As starting points we use the values measured by Chen *et al.* on suspended CVD graphene:  $\chi_G = -(4.4 \pm 0.3) \times 10^{-2} \text{ cm}^{-1}/K$ ,  $\chi_{2D} = -(7.2 \pm 0.2) \times 10^{-2} \text{ cm}^{-1}/K$  (Chen et al., 2011). Other measurements report lower values (Calizo et al., 2007), and hence, higher thermal conductivities (Balandin et al., 2008). These values were not used because they were measured on supported graphene where the different thermal

expansion coefficients of graphene and the substrate could be more of an issue. Since these temperature related shifts happen because of phonon anharmonicities, they may have some strain dependence. The Anti-Stokes to Stokes ratio could be used as an alternative, anharmonicity independent temperature measurement. However, we found that these measurements were not useful as they took too long and were too hard to interpret. The extraction of the temperature is complicated by the lack of a universal room temperature phonon energy to measure the energy shifts from. As pressure is applied to the graphene it becomes strained and the zero temperature phonon energies shift. To circumvent this problem two spectra are needed to measure the temperature: One at a lower power,  $P_{lo}$ , and one at a higher power,  $P_{hi}$ . Assuming that the thermal resistance,  $R = \frac{\Delta T}{P}$  where P is the absorbed power, is constant gives

*put in several steps here.*

*Also, how are you dealing with changes in  $\chi$  due to pressure?*

You have  $\Delta\omega$  due to temperature and  $\Delta\omega$  due to pressure.

$$T_M = T_{hi} - T_0 = \frac{\Delta\omega}{\chi} \frac{P_{hi}}{P_{hi} - P_{lo}}, \quad (5.1)$$

where  $T_0$  is ambient temperature and  $T_M$  is referred to as the measured temperature.

The corresponding measured thermal resistance is  $R_M = T_M/P_{hi}$ . The measured values do not represent the temperature at the center of the microchamber. They are weighted averages over the finite spot of the laser beam.

The heat transfer model described in Appendix D is used to extract the thermal parameters from the measured temperatures. The model depends on the thermal conductivities of the suspended graphene,  $\kappa_{SS}$ , and the supported graphene,  $\kappa_{SP} = (579 \pm 34) \text{ W/m-K}$  (Seol et al., 2010), as well as the interface thermal conductivities to the gas,  $g_G$ , and to the substrate  $g_S = (50 \pm 13) \text{ MW/m}^2\text{-K}$  (Mak et al., 2010). An example temperature distribution predicted by this model is shown in figure 5.2. As one might expect, the temperature rise is the greatest in the center of the microchamber where the laser is positioned. At the edge of the microchamber the

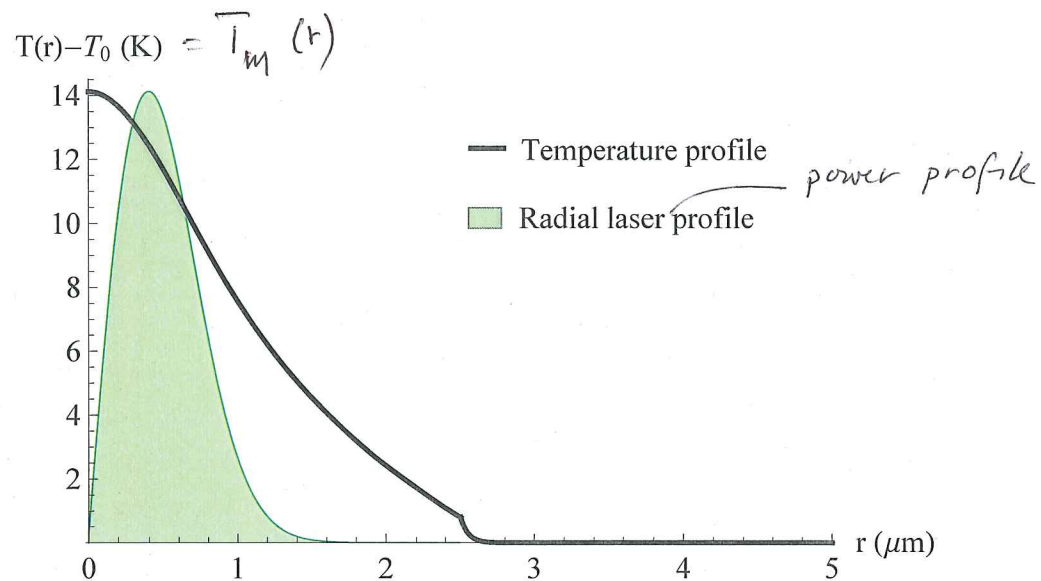


Figure 5.2: Theoretical temperature distribution in a graphene sealed microchamber heated by a centered laser. The black curve shows the temperature increase for a  $5 \mu\text{m}$  diameter microchamber assuming that  $\kappa_{SS} = 2000 \text{ W/m-K}$  and  $g_G = 0.03 \text{ MW/m}^2\text{-K}$  (Chen et al., 2011). The radial profile of the 1.5 mW laser heat source with a  $0.66 \mu\text{m}$  waste *wrist* is overlaid in green.

slope is discontinuous due to the change in thermal conductivity. Where the thermal conductivity is lower it takes a larger temperature gradient to conduct the same heat energy. The green shaded region represents the radial envelope of the excitation profile. It illustrates that  $T_M$  is not the temperature rise at the center of the hole but is rather an average over a radial window. Appendix D describes how  $T_M$  can be used to find the thermal parameters.

The samples described in Table 5.1 were measured by taking Raman spectra with multiple excitation powers across a range of pressures. The number of layers was found using Raman spectroscopy and optical interference, the radius and hole depths

How do you achieve strain  
in a non-sealed  
chamber?

98

Samples	NL	Radius	Depth	$\epsilon_{max}$	Fabrication	Sealed?
FFF	1	( $3.09 \pm 0.04$ ) $\mu\text{m}$	> 5 $\mu\text{m}$	1.2 %	Transferred	no
SB07-1	1	( $2.74 \pm 0.08$ ) $\mu\text{m}$	$\simeq 230 \text{ nm}$	1.1 %	Exfoliated	yes
SB08-2	2	( $1.52 \pm 0.07$ ) $\mu\text{m}$	> 3 $\mu\text{m}$	0.46 %	Exfoliated	yes
SB03-2	3	( $4.99 \pm 0.01$ ) $\mu\text{m}$	> 5 $\mu\text{m}$	0.77 %	Exfoliated	yes

Table 5.1: Details of the samples used in thermal conductivity measurements. NL refers to the number of layers and  $\epsilon_{max}$  is the maximum strain.

were measured using low force contact mode AFM, and the maximum strain was calculated using Hencky's model (Hencky, 1915). Device fabrication was either done using the standard mechanical exfoliation technique or by using a polymer based aligned transfer technique (Goossens, 2013). Pressures were decreased in increments from 0.69 MPa to -0.1 MPa and then increased back to 0.69 in inter-spaced increments to monitor for any hysteretic response. These measurements allowed for the extraction of the pressure dependent measured thermal resistance.

### 5.2.2 Data analysis

This section details the analysis done to determine the measured thermal resistances from the Raman spectra.

Peak positions were found by fitting the measured spectra to representative spectral shapes. The G peak was fit to a single Lorentzian for all four samples. Fitting the 2D peak was more complicated because the peak shape depends on the number of layers. For suspended monolayer graphene the 2D peak is best fit by two Lorentzians with equal widths separated by 14 wavenumbers (Berciaud et al., 2013). To limit the number of fitting parameters, the ratio of the peak amplitudes was taken as 3.44, the average of less restricted best fits. For bilayer graphene the 2D peak is best fit by 4 Lorentzians with equal widths (Ferrari et al., 2006; Malard et al., 2007). The fitting

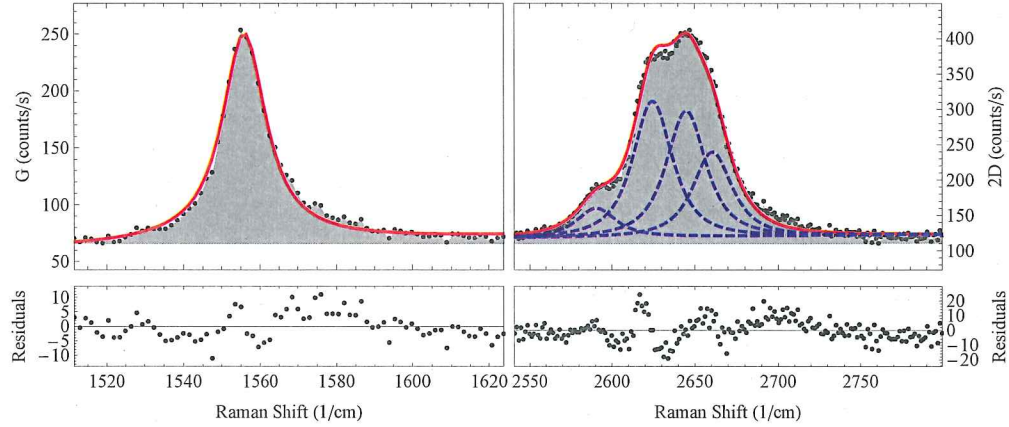


Figure 5.3: A representative fit to the Raman spectra taken at the center of bilayer sample SB08-2 using 2 mW of incident power at 0.69 MPa of gauge pressure. The restricted four Lorentzian fit to the 2D spectra matches the data well.

parameters were restricted to an amplitude, a width, and a position by setting the separation between peaks and the relative amplitudes between peaks based on the average of less restricted best fits. An example of the best fit to a bilayer spectra is shown in Figure 5.3 showing good agreement between the spectra measured at 0.69 MPa and the fitting function. Since there is no well-excepted form for the trilayer 2D band, the temperatures were only determined from the G band data for sample SB03-2. The extracted peak positions were used to analyze the response of the system to pressure and heating.

Figure 5.4 shows the best fit positions of the G and 2D bands as a function of pressure for bilayer sample SB08-2. As described in detail in Chapter 4, the overarching response is governed by the linear dependence of the Raman bands on strain. The strain, in turn, scales roughly as  $(P - P_0)^{2/3}$  where  $P_0$  is the pressure inside the microchamber. The data in the figure is fit by the expected pressure dependence and the extracted value of  $P_0$  is indicated by the black vertical line. Samples SB07-1,

Show data for all 4 samples

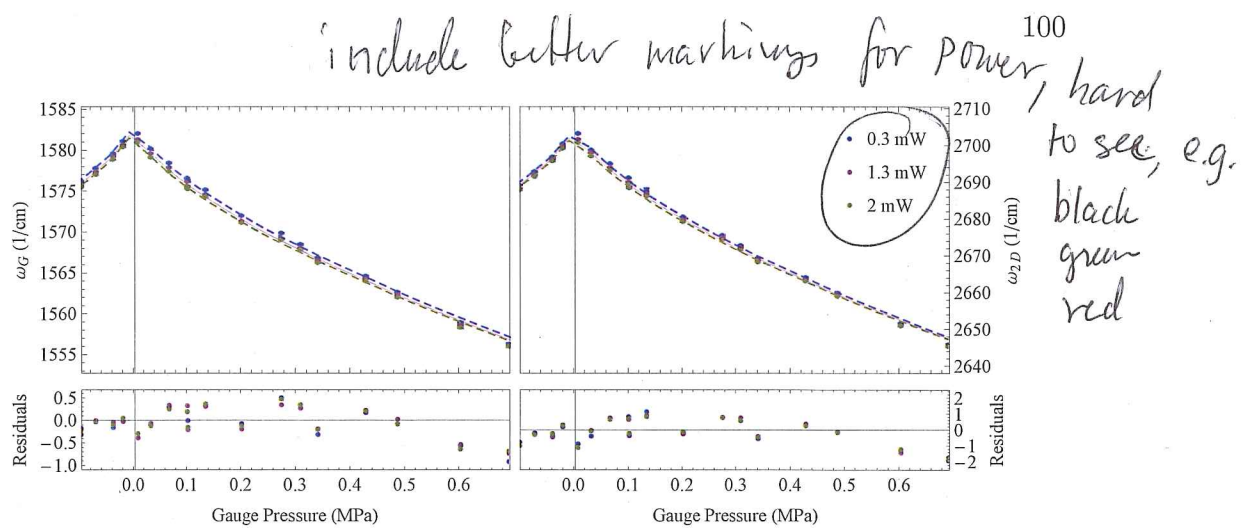


Figure 5.4: The peak positions measured as a function of applied pressure with three different laser excitation powers for bilayer sample SB08-2. The peak positions are fit to the expected  $(P - P_0)^{2/3}$  behavior and the best fit value for  $P_0$  is indicated by the black vertical line. Increasing laser excitation power systematically red shifts the peak positions. *different colors, different power...*

SB08-2, and SB03-2 all exhibit this type of pressure dependent response. Sample FFF, on the other hand, exhibits no pressure response indicating that the membrane is leaky. Thus, this sample is only sensitive to pressure effects. The effects of laser heating are hidden in the fine structure. Spectra taken at higher laser powers exhibit systematically lower peak positions due to heating.

The use of Equation 5.1 to calculate the temperatures from the peak shifts is complicated by optical interference. As shown in Figure 5.5, the measured temperatures for sample SB07-1 exhibit an oscillatory behavior in pressure that is correlated with similar oscillations in the measured G and 2D areas. This suggests that the observed behavior is driven by optical interference in the excitation beam. As overpressure is applied to the graphene it is pushed into the microchamber moving it from a point where the excitation undergoes destructive interference, to a point of constructive

*you are contradicting yourself later with interference*

interference, and then back to a point of destructive interference. As the interference changes, the amount of power heating the graphene changes, and thus, so does the temperature. The interference interpretation is supported by the agreement between the number of interference minimum and the expected displacement at the center of the graphene. Minimum are expected every half wavelength and from -0.1 MPa to 0.69 MPa, the graphene displaces by 508 nm or roughly one wavelength consistent with the two minimum in Figure 5.5. The interference in SB07-1 is the strongest, but all of the other devices exhibit similar interference phenomena. The Rayleigh range of the focused beam is  $\sim 2.7 \mu\text{m}$  indicating that even microchambers with depths of  $8 \mu\text{m}$  might be expected to exhibit weak interference effects. Interestingly, even leaky sample FFF shows very slight signs of interference probably due to the nonlinearity of the pressure deflection curve. In the low pressure regime small pressure changes cause relatively large deflections; for FFF a differential pressure of only 0.001 MPa would cause a deflection of 40 nm. To correctly interpret the thermal response of the system, this interference must be accounted for.

why, it shows no pressure dependence  
or uncovered

The optical interference of the excitation beam can be estimated from the oscillatory behavior of the Raman signal. The Raman signal is driven by the product of the optical interference of the incident beam and the outgoing, inelastically scattered light. Approximating the system as a plane wave incident on a perfect mirror, the product of these two terms is  $4 \sin^2(kz) \sin^2(k_R z)$  where  $z$  is the distance of the graphene above the mirror,  $k$  is the spatial frequency of the laser excitation, and  $k_R$  is the spatial frequency of the inelastically scattered light. The perfect mirror approximation is reasonable for silicon in the visible. Using silicon's optical constants from Palik *et al.* (Palik and Ward, 1991) reproduces the approximate behavior with a negligible 2 % constant offset. The oscillations in the measured temperature, however, are only due to the interference in the incident beam. The  $2 \sin^2(kz)$  component. The fact

; the

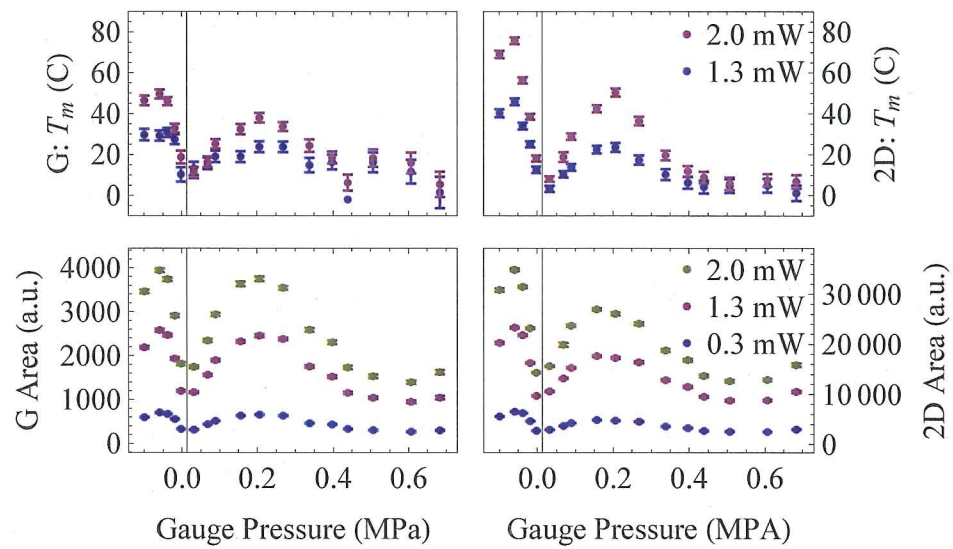


Figure 5.5: A comparison of the temperatures calculated from the shifts of the G peak (top, left) and the shifts of the 2D peak (top, right) with the measured areas of the G peak (bottom, left) and the 2D peak (bottom, right). Measurements were taken on monolayer sealed sample SB07-1. The oscillatory behavior in all four plots suggests that the observed behavior is a result of optical interference.

that the exact depths of the microchambers are not known and that the interference is in a Gaussian beam and not a plane wave makes a direct calculation of the incident power from the oscillations in the Raman areas impractical. Instead, we approximate  $4 \sin^2(kz) \sin^2(k_R z) \simeq 4 \sin^2(kz) = (\text{int})^2$  allowing an estimation of the interference in the excitation beam.

There is a constant offset underlying the oscillations in the G and 2D areas as shown in Figure 5.5. The signal contributing to this offset is believed to be generated by light which is not interfering. This could be a result of a rough silicon back plane or from the divergence of the beam. Accounting for this offset, the interference is calculated as

$$\text{Area} = P_i A + P_i B \text{int}^2 / 4 \rightarrow \text{int} = 2 \sqrt{\frac{\text{Area}/P_i - A}{B}},$$

I don't understand what you are doing here  
What areas are these? What is A, B?

where  $P_i$  is the power of the incident beam and  $A$  and  $A + B$  are the minimum and the maximum of the  $P_i$  normalized areas, respectively. The intensity of the incident beam at the sample is then given by  $P_i(A+B \text{int})/(A+B)$ . Using this correction, the thermal resistances can be calculated from the measured temperatures. The resulting  $R_M$  should be independent of interference effects up to the approximations used.

Accurate determinations of the measured thermal resistances are enabled by redundant measurements. For samples FFF, SB07-1, and SB08-2 both the G and 2D shifts can be used to calculate  $R_M$ . The values of  $\chi$  reported by Chen *et al.* (Chen *et al.*, 2011) provided good agreement between G and 2D data for sample SB08-2. However, for sample FFF, a slight offset was required to achieve good agreement. The values of  $\chi$  for the G and 2D peaks needed to be increased and decreased by  $0.6 \times 10^{-2} \text{ cm}^{-1}/\text{K}$  respectively. For sample SB07-1, the G and 2D measurements are presented separately. Samples SB07-1, SB08-2, and SB03-2 were measured at three

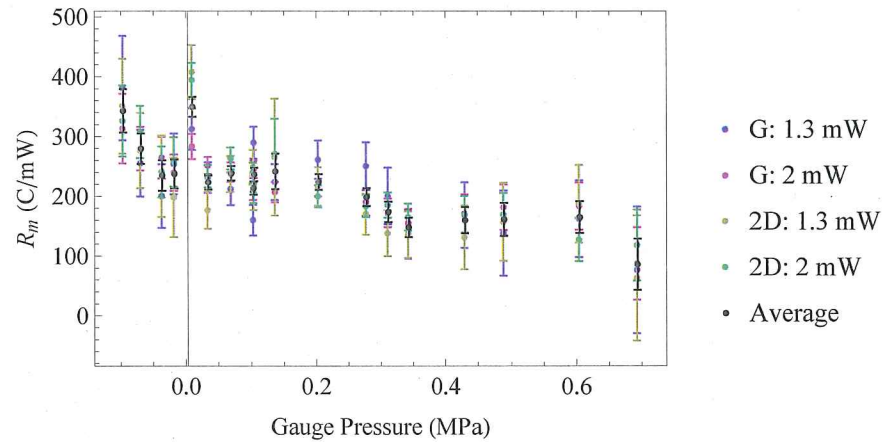


Figure 5.6: The average measured thermal resistance of bilayer sample SB08-2. The four different measurements used to calculate the average are in good agreement. The black vertical line is positioned at  $P_0$ .

different powers providing two additional measurements of  $R_M$ . Averaging all of the redundant measurements provides higher certainties. Figure 5.6 shows an example of the averaged  $R_M$  data. The individual  $R_M$  measurements are in good agreement, justifying the averaging.

In summary, the measured thermal resistance is calculated by fitting the measured spectra, using the heating shifts to determine temperatures, correcting for optical interference, and averaging over redundant measurements. The general trends in the measurements are discussed in the following section.

### 5.2.3 Discussion

Figure 5.7 shows the thermal resistance measured on the four samples. After scaling the leaky monolayer (FFF) measurements by 0.28, they agree well with the measured of the sealed bilayer (SB08-2) and the sealed trilayer (SB03-2). They all exhibit a

scaling what  
parameters  
why?

monotonic decrease in  $R_M$  with increased pressure. The lack of symmetry about the pressure inside the microchamber ( $P_0 \approx 0$ ) indicates that the trend is unrelated to the strain in the graphene. This is further supported by the agreement between the sealed and leaky microchambers. The sealed monolayer graphene measurements, on the other hand, do display symmetry about  $P_0$ . However, the correlation between these features and the optical interference in Figure 5.5 indicates that these features could be attributed to imperfect interference corrections. In fact, this device should be most sensitive to the approximations made in correcting the optical interference since the sealed monolayer is the most shallow and undergoes the most interference. Thus, for monolayer graphene the observed trend is indecipherable and for bilayer and trilayer graphene in the strain regions measured (see Table 5.1), there is no evidence for strain dependent thermal conductivity. Additionally, no measurements show the significant decrease in  $R_M$  at high pressure which would indicate the predicted strain-induced transition to divergent thermal conductivity (Bonini et al., 2012; Pereira and Donadio, 2013).

The pressure dependent measured thermal resistances could originate from thermal conduction to the gas, from viscous damping of the ZA phonons, or from both. To test if the observed behavior can be reasonably attributed only to the thermal conduction the gas, viscous damping was neglected and the interface thermal conductivity to the gas,  $g_G$ , was fit to the data following Appendix D. Assuming that  $g_G = 0 \text{ W/m}^2\text{-K}$  in a vacuum, the in-plane thermal conductivity was extracted from the measurement with the largest  $R_M$  measured at vacuum. This gave  $\kappa_S S = 800 \pm 100 \text{ W/m-K}$ ,  $\kappa_S S = 1300 \pm 100 \text{ W/m-K}$ ,  $\kappa_S S = 770 \pm 30 \text{ W/m-K}$  for the bilayer, trilayer, and leaky monolayer samples respectively. One sigma confidence intervals were calculated using a Monte-Carlo technique which accounts for all known uncertainties. The results are shown in Figure 5.8

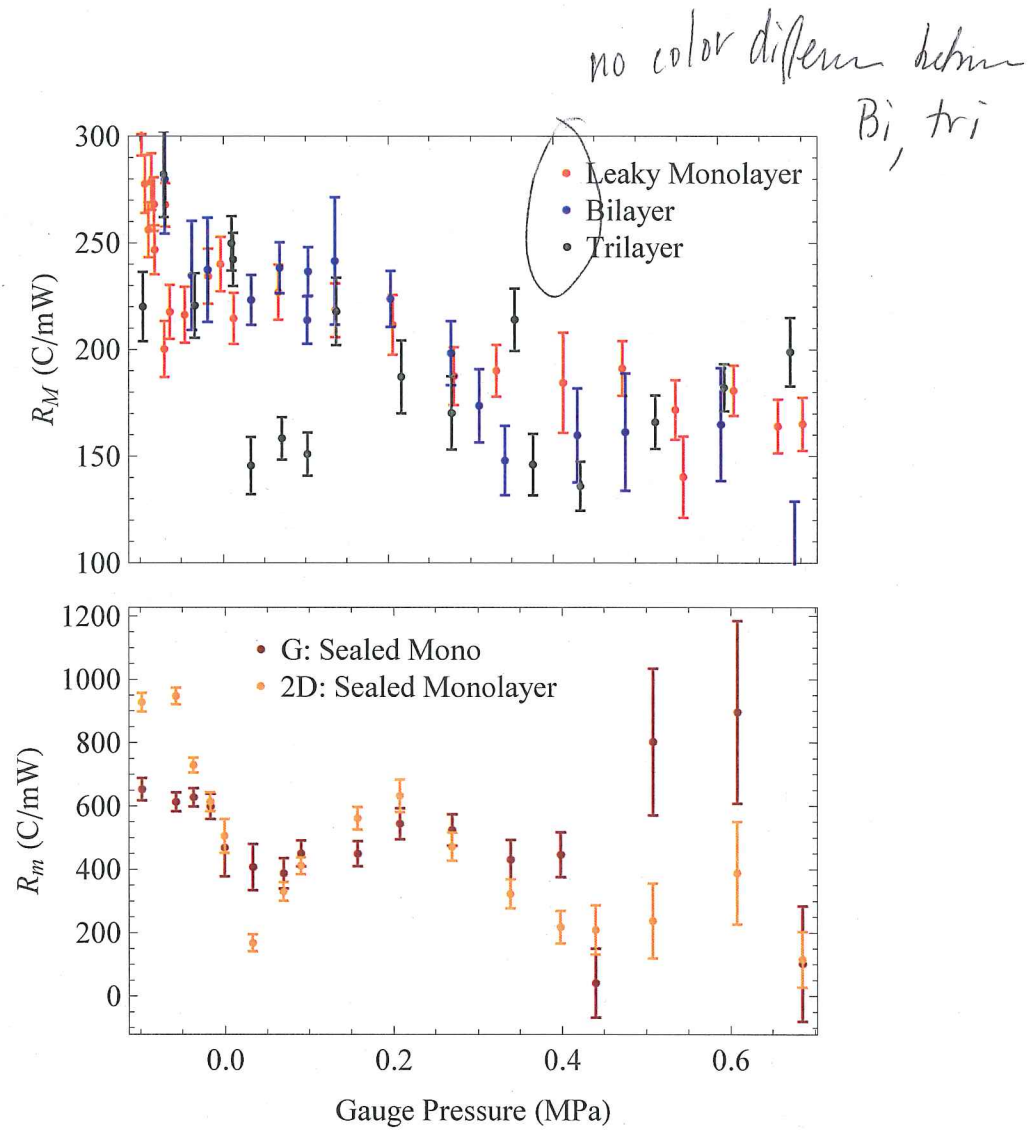


Figure 5.7: Comparison of the pressure dependent measured thermal resistances of sealed monolayer (SB07-1), bilayer (SB08-2), and trilayer (SB03-2) graphene as well as leaky monolayer (FFF) graphene. The thermal resistances of the leaky monolayer was scaled by a factor of 0.28 for easier comparison. Data for the sealed monolayer graphene is plotted separately to better see the trends in the data.

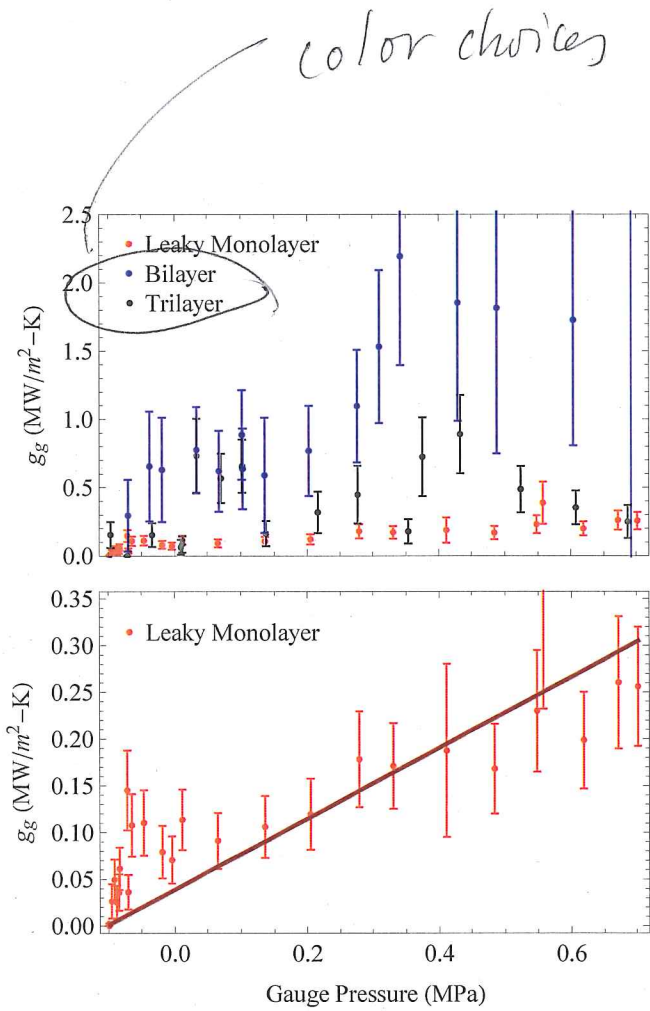


Figure 5.8: Assuming that the in plane thermal conductivity is constant, the  $R_M$  in Figure 5.7 were used to determine the interface thermal conductivity to the gas. The top plot compares the values for a leaky monolayer (FFF), a sealed bilayer (SB08-2), and a sealed trilayer (SB03-2) while the bottom plot shows only the leaky monolayer data fit to a line.

The behavior of the interface thermal conductivity of the leaky monolayer is different than the sealed bilayer and trilayer samples. For pressures greater than ambient pressure, the interface thermal conductivity of the leaky monolayer increases roughly linearly with pressure. This linear trend is expected based on a kinematic model (Chen et al., 2011). At higher pressures there are more atoms in the gas available to conduct heat away from the sample. Additionally, the ambient pressure value of  $g_g \approx 0.1 \text{ MW/m}^2\text{-K}$  is in fair agreement with the previously measured value for graphene in air of  $g_g = 0.029 + 0.051 / - 0.029 \text{ MW/m}^2\text{-K}$  (Chen et al., 2011). Thus, other than the excess observed around  $-0.1 \text{ MPa}$ , the thermal response of the leaky monolayer is consistent with thermal conduction to the gas. That excess is not yet understood. Bilayer and trilayer graphene exhibit different behavior. Their interface thermal conductivity is higher and behaves less linearly than the leaky monolayer. This is probably due to the gas sealed inside of these microchambers. For low applied gas pressures the gas in the microchamber conducts much more heat than the gas above the microchamber resulting in a fairly flat pressure response in  $g_g$ . For larger pressures, the conduction to the gas above dominates the conduction to the gas below and a stronger pressure response should occur. The flattening out of the pressure response at the highest pressures is not yet understood.

#### 5.2.4 Conclusions

Strain and pressure dependent thermal conductivity measurements were performed on monolayer, bilayer, and trilayer graphene to gain insight into the atypical thermal conductivity in FLG. Strain and pressure are expected to modify the quadratic ZA phonon, believed to be the main contributor to the high thermal conductivity in strained graphene. We found that sealed bilayer and trilayer graphene devices as well as leaky monolayer graphene exhibits measured thermal resistances which decrease

is this one or the other  
or one, i.e. the other?

Why?

109

monotonically with pressure. This behavior is consistent with heat conduction to the gas or viscous damping of the ZA phonons. Assuming a constant in plane thermal conductivity showed that the leaky monolayer results were consistent with heat conduction to the gas. The interpretation of the sealed bilayer and trilayer samples was complicated by the gas sealed inside of the microchambers. Future measurements of leaky bilayer and leaky trilayer samples could be used to ease the interpretation. The results for monolayer graphene were indecipherable because of optical interference. In future measurements microchambers should be fabricated much deeper to eliminate these effects. We did not observe the predicted strain induced transition to divergent thermal conductivity (Bonini et al., 2012; Pereira and Donadio, 2013) in any of our devices. This may be because we did not reach high enough strains, because the strain distributions which develop in graphene sealed microchambers are not suitable, or because the predictions are incorrect.

